applied optics

Radiative transfer simulations of the two-dimensional ocean glint reflectance and determination of the sea surface roughness

Zhenyi Lin,[1,*] Wei Li,[1] Charles Gatebe,[2,4] Rajesh Poudyal,[3,4] and Knut Stamnes[1]

[1]Department of Physics and Engineering Physics, Stevens Institute of Technology, Hoboken, New Jersey 07030, USA
[2]Universities Space Research Association, Columbia, Maryland 20146, USA
[3]Science Systems and Applications, Inc., Lanham, Maryland 20706, USA
[4]NASA Goddard Space Flight Center, Greenbelt, Maryland 20771, USA
*Corresponding author: lzhenyi@stevens.edu

An optimized discrete-ordinate radiative transfer model (DISORT3) with a pseudo-two-dimensional bidirectional reflectance distribution function (BRDF) is used to simulate and validate ocean glint reflectances at an infrared wavelength (1036 nm) by matching model results with a complete set of BRDF measurements obtained from the NASA cloud absorption radiometer (CAR) deployed on an aircraft. The surface roughness is then obtained through a retrieval algorithm and is used to extend the simulation into the visible spectral range where diffuse reflectance becomes important. In general, the simulated reflectances and surface roughness information are in good agreement with the measurements, and the diffuse reflectance in the visible, ignored in current glint algorithms, is shown to be important. The successful implementation of this new treatment of ocean glint reflectance and surface roughness in DISORT3 will help improve glint correction algorithms in current and future ocean color remote sensing applications. © 2016 Optical Society of America

1. INTRODUCTION

Satellite remote sensing under glint conditions remains a challenging problem [1]. The contribution from glint to the radiance measured at the top of the atmosphere (TOA) is large enough to dominate the sensor-received signals. Algorithms developed for current satellite sensors [e.g., the sea-viewing wide field of view sensor (SeaWiFS), the moderate-resolution imaging spectroradiometer (MODIS), the medium resolution imaging spectrometer (MERIS), the polarization and directionality of Earth reflectances instrument, and the global imager], use different correction algorithms [2–4] that all follow the same principle: estimate the glint contribution based on a statistical glint model and a direct beam reflectance and then remove its contribution from the signal received by the sensor.

Despite the use of polynomial approximations [3,5,6], most correction methods are based on a glint model with a statistical water surface slope distribution according to a simple linear or exponential relation between mean values of slope variances and wind speeds (upwind/crosswind). Ever since Cox and Munk presented the first glint model [7] based on

photographic measurements in 1954, a variety of studies, including nonlinear parameterizations, have been done to upgrade this model so as to improve satellite retrieval quality [8–11]. However, the quality of the statistical distribution depends on the accuracy of the measurements of wind speed and direction, and in practice the values of surface slope variances always deviate from the statistical mean values and are spread out over a wider range [9]. There are also biases in such parameterizations caused by variations in the air–water temperature difference [12] and atmospheric stability [13].

To analyze remotely sensed radiances obtained by instruments such as SeaWiFS, MODIS, and MERIS, NASA has developed a comprehensive data analysis software package (SeaWiFS Data Analysis System, SeaDAS), which performs a number of tasks, including cloud screening and calibration, required to convert the raw satellite signals into calibrated TOA radiances. In addition, the SeaDAS software package has tools for quantifying and removing the atmospheric contribution to the TOA radiance (atmospheric correction) as well as contributions from whitecaps and sun glint due to reflections from the ocean surface [14].

The sun glint radiance at the TOA can be expressed as a function of the following variables,

$$I_{\text{glint}}^{\text{TOA}} \equiv I_{\text{glint}}^{\text{TOA}}(\mu_0, \mu, \Delta\phi, W, \Delta\phi_W, \text{AM}, \tau_{\text{tot}}, \lambda), \quad \text{(1)}$$

where μ_0, μ, and $\Delta\phi$ define the sun-satellite geometry, W is the wind speed, $\Delta\phi_W$ is the wind direction, and λ the wavelength. The atmosphere is characterized by its total optical depth τ_{tot}, and the choice of an aerosol model.

In the SeaDAS algorithm (and similar algorithms) a sun glint flag is activated to mask out pixels for which the reflectance or bidirectional reflectance distribution function (BRDF), exceeds a certain threshold. If the reflectance for a given pixel is above the threshold, the signal is not processed. If the reflectance is below the threshold, a directly transmitted radiance approach is used to calculate the TOA sun glint radiance in the SeaDAS algorithm. Thus, it is computed assuming that the direct beam and its reflected portion only experience exponential attenuation through the atmosphere [2], that is,

$$I_{\text{glint}}^{\text{TOA}}(\mu_0, \mu, \Delta\phi) = F_0(\lambda) T_0(\lambda) T(\lambda) I_{GN}, \quad \text{(2)}$$

$$T_0(\lambda) T(\lambda) = \exp\left\{-[\tau_M(\lambda) + \tau_A(\lambda)]\left(\frac{1}{\mu_0} + \frac{1}{\mu}\right)\right\}, \quad \text{(3)}$$

where the normalized sun glint radiance I_{GN} is the radiance that would result in the absence of the atmosphere if the incident solar irradiance were $F_0 = 1$, and where τ_M and τ_A ($\tau_{\text{tot}} = \tau_M + \tau_A$) are the Rayleigh (molecular) and aerosol optical thicknesses. The downward diffuse incident light (sunlight being multiply scattered by atmospheric molecules and aerosols before hitting the rough sea surface) also contributes to the upward reflectance. In the SeaDAS algorithm, such diffuse light reflectance that accounts for the effect of ocean surface roughness has been included only in the Rayleigh lookup tables [15].

Radiative transfer (RT) simulations provide an alternative way to look at the glint problem more completely [16–18]. An RT model can be used to quantify contributions not only from the sun glint, but also from the multiply scattered radiance in an accurate manner [19]. For instance, Gao *et al.* developed an atmospheric correction algorithm [20,21] that uses lookup tables generated with a vector radiative transfer code of Ahmad and Fraser [22] and takes into account sea surface roughness for diffuse light. The data produced by RT model simulations can be used to test current correction methods and explore the potential for extending remote sensing into strong glint situations that the current SeaDAS algorithm is masking out.

Many RT models (such as DISORT [23–25], SCIATRAN [26], SOS [27], LIDORT [28], etc.) have already implemented a rough ocean surface to mimic the BRDF. However, plane parallel RT models assume that the BRDF depends only on the difference in azimuth between the sun–sensor directions. Hence they are intrinsically one-dimensional, and therefore incapable of simulating the directional dependence of realistic slope distributions that may be better represented by a two-dimensional (2D) Gaussian function. Another problem is that few studies have focused on validation of such BRDF implementations due to the general lack of a complete set of ocean reflectance measurements that would be suitable for testing purposes.

To overcome these difficulties and thereby enable more realistic simulations of ocean glint reflectance, we developed a RT model with a pseudo-2D BRDF that accurately represents the nature of the sea surface slope distribution. To validate the RT simulations we used reflectance measurements obtained by an instrument deployed on a NASA airplane. Our goal was to match simulated reflectances with those measured by the cloud absorption radiometer (CAR) instrument deployed on the NASA airplane, and to use RT simulations as a forward model to invert the measured reflectance in order to retrieve wind direction, sea surface slopes in the crosswind and upwind direction, and aerosol optical thickness. These parameters are important for atmospheric correction, which is the largest source of error and uncertainty in determining water-leaving radiance from space. Finally, we examined the influence of the diffuse light reflectance to study its importance.

2. RADIATIVE TRANSFER MODEL

The discrete ordinate radiative transfer model implemented numerically in the DISORT code [25] provides accurate computations of singly and multiply scattered radiances at arbitrary locations and in arbitrary directions in a turbid medium. The DISORT code has been used in a great variety of studies including remote sensing applications. The latest version of DISORT (hereafter referred to as DISORT3), updated in 2015 with improved BRDF capabilities [23], was modified and optimized to simulate the two-dimensional nature of the surface reflectance in this study. The DISORT3 code can be obtained from the following web site: http://lllab.phy .stevens.edu/disort/ [29].

A. Atmospheric Input and Output
To minimize the influence of light backscattered from the water, we first looked at a wavelength in the near infrared at 1036 nm, where absorption by water is strong, and adopted two atmospheric layers: one Rayleigh (molecular) layer (2–10 km) and one layer with aerosols and molecules homogeneously mixed (0–2 km). Based on the US standard atmosphere [30], the single scattering albedo at 1036 nm is $\varpi_{\text{mol}} = 0.9610$ in the upper layer (molecules only) and the upper layer optical thickness is $\tau_{\text{mol}} = 0.00645$. In the lower layer, we adopted an aerosol model implemented in SeaDAS [31]. The inherent optical properties of aerosols and molecules were then combined to give a "mixed" single scattering albedo $\varpi_{\text{mix}} = (\sigma_{\text{mol}} + \sigma_{\text{aer}})/(k_{\text{mol}} + k_{\text{aer}}) = 0.9772$, where σ_{mol} and σ_{aer} are scattering coefficients, and k_{mol} and k_{aer} are extinction coefficients for molecules and aerosols, respectively.

The simulated atmospheric output is the radiance $I(\tau, \mu, \phi)$ in arbitrary directions (μ, ϕ). However, for comparison with measurements, we used the reflectance defined as $R(\tau, \mu, \phi) = \pi I(\tau, \mu, \phi)/\mu_0 F_0$, which is a function of μ (cosine of the view zenith angle, θ), ϕ (azimuth angle), τ (optical thickness at aircraft altitude), μ_0 (cosine of the solar zenith angle, θ_0), and F_0 (the extraterrestrial solar spectral irradiance). Note that this reflectance is defined such that it would represent the reflected irradiance normalized by the TOA incident irradiance $\mu_0 F_0$ if the intensity were to be isotropic.

B. Pseudo-Two-Dimensional BRDF

At the bottom of the atmosphere ($\tau = \tau_{atm}$), the upward reflected radiance $I_{up,refl}(\tau_{atm}, \mu', \phi')$ is connected to the downward incident diffuse radiance $I_{down,inc}(\tau_{atm}, \mu, \phi)$ and the attenuated direct radiance $F_0 e^{-\tau_{atm}/\mu_0}$ through the sea surface reflection that is described by the BRDF $\rho(\mu, \mu', \Delta\phi)$,

$$I_{up,refl}(\tau_{atm}, \mu', \phi')$$
$$= \mu_0 \rho(\mu_0, \mu', \phi') F_0 e^{-\tau_{atm}/\mu_0}$$
$$+ \int_0^{2\pi} \int_0^1 \mu\rho(\mu, \mu', \Delta\phi) I_{down,inc}(\tau_{atm}, \mu, \phi) d\mu d\phi, \quad \textbf{(4)}$$

where $\Delta\phi = \phi' - \phi$, and the solar azimuth angle was set to $\phi_0 = 0°$ so that $\Delta\phi = \phi' - \phi_0 = \phi'$ for the direct beam reflection $\rho(\mu_0, \mu', \phi')$.

The BRDF $\rho(\mu, \mu', \Delta\phi')$ is given as

$$\rho(\mu, \mu', \Delta\phi) = \frac{1}{4\mu'\mu(\mu_n)^4} \cdot p(\mu_n, \sigma) \cdot r(\cos\Theta, n) \cdot s(\mu, \mu', \sigma),$$
$$\textbf{(5)}$$

$$\mu_n = \frac{\mu + \mu'}{\sqrt{2(1 - \cos\Theta)}}, \quad \textbf{(6)}$$

$$\cos\Theta = -\mu\mu' + \sqrt{1 - \mu^2}\sqrt{1 - \mu'^2}\cos(\Delta\phi), \quad \textbf{(7)}$$

where μ is cosine of the view zenith angle for the incident light, μ' is cosine of the view zenith angle for the reflected light, $\Delta\phi$ is the relative azimuth angle, Θ is the scattering angle, μ_n is the cosine of θ_n, the angle between the ocean wave facet normal and the vertical direction. In Eq. (5), $r(\cos\Theta, n)$ is the Fresnel reflectance of unpolarized light, $s(\mu, \mu', \sigma)$ describes the effect of shadowing, and $p(\mu_n, \sigma)$ is the surface slope distribution (assumed to be a 1D or a 2D Gaussian).

In DISORT3, the radiance $I(\tau, \mu, \phi)$ and the BRDF $\rho(\mu, \mu', \Delta\phi)$ are expanded into a Fourier cosine series to isolate the azimuth dependence, which in 1D depends only on the difference $\Delta\phi = \phi' - \phi$ in azimuth between the direction of incidence (θ', ϕ') and observation (θ, ϕ). The pseudo-two-dimensional BRDF is an approximation that employs a 2D BRDF to compute the direct beam reflectance, but employs the Fourier expanded 1D BRDF to compute the reflectance of the diffuse, multiply scattered light. The implementation is based on a postprocessing step which corrects the direct beam reflectance (1D → 2D) after the call to the RT model. This postprocessing method is similar to the Nakajima-Tanaka (NT) correction [32], which retains the multiply scattered radiance, but corrects the singly scattered radiance without considering boundary reflection. In DISORT3, we improved the NT procedure by adding a BRDF correction [23] and here we follow the same strategy by adding a 2D BRDF correction. Hence, the correction term for radiance $I_{sscorr}(\hat{\tau}, \pm\mu, \phi)$ can be written as

$$I_{ss\,corr}(\hat{\tau}, \pm\mu, \phi) = I_{ss}^*(\hat{\tau}, \pm\mu, \phi) - \tilde{I}_{ss}^*(\hat{\tau}, \pm\mu, \phi)$$
$$+ \mu_0 F_0 \{\rho_{2D}(\mu, \phi; -\mu_0, \phi_0)$$
$$- \rho_{1D}(\mu, \phi; -\mu_0, \phi_0)\} e^{-\frac{\hat{\tau}_b}{\mu_0} + \frac{\hat{\tau} - \hat{\tau}_b}{\mu}}. \quad \textbf{(8)}$$

Here, $\hat{\tau}$ and $\hat{\tau}_b$ are the scaled optical thicknesses at the height of interest and the lower boundary, respectively [23,32]. On the right-hand side of Eq. (8), $I_{ss}^*(\hat{\tau}, \pm\mu, \phi) - \tilde{I}_{ss}^*(\hat{\tau}, \pm\mu, \phi)$ is the original NT correction [32], $\rho_{2D}(\mu, \phi; -\mu_0, \phi_0)$ is the new 2D BRDF used to compute the 2D single scattering contribution, $\rho_{1D}(\mu, \phi; -\mu_0, \phi_0)$ is the Fourier expanded 1D BRDF used to compute the approximate multiple scattering contribution, and $e^{-\frac{\hat{\tau}_b}{\mu_0} + \frac{\hat{\tau} - \hat{\tau}_b}{\mu}}$ is the beam attenuation coefficient.

For multiply scattered light, we use a 1D Gaussian surface slope distribution given by [7]

$$p(\mu_n, \sigma) = \frac{1}{\pi\sigma^2} \exp\left(-\frac{\tan^2\theta_n}{\sigma^2}\right), \quad \textbf{(9)}$$

where σ^2 is the variance of the slope distribution. The 1D BRDF given by Eqs. (5)–(7) and (9) is suitable for describing "sky glint," that is, the reflectance of downward diffuse light from a rough water surface, because multiple scattering in the atmosphere has made the radiation field approximately 1D, implying that 2D BRDF effects become relatively unimportant for the reflected diffuse skylight [33].

Similarly, the slope distribution for a 2D Gaussian surface is given by [7]

$$p(z_x, z_y) = \frac{1}{2\pi\sigma_x\sigma_y} \exp\left[-\frac{1}{2}\left(\frac{z_x^2}{\sigma_x^2} + \frac{z_y^2}{\sigma_y^2}\right)\right]. \quad \textbf{(10)}$$

Here the rough ocean surface is assumed to be characterized by a Gaussian random height distribution $z = f(x, y)$ with mean height $\langle z \rangle = \langle f(x, y) \rangle = 0$, and the slopes are given by

$$z_x = \frac{\partial z}{\partial x} = \frac{\partial f(x, y)}{\partial x} = \sin\Delta\phi \tan\theta_n, \quad \textbf{(11)}$$

$$z_y = \frac{\partial z}{\partial y} = \frac{\partial f(x, y)}{\partial y} = \cos\Delta\phi \tan\theta_n, \quad \textbf{(12)}$$

where θ_n is the tilt angle and $\Delta\phi$ the relative azimuth angle of the surface facet. For an isotropic (1D) slope distribution ($\sigma_x^2 = \sigma_y^2 = \frac{\sigma^2}{2}$), Eq. (10) reduces to Eq. (9), which is widely used in remote sensing applications to represent the slope statistics of water waves with the numerical value of the slope variance parameterized in terms of wind speed.

Gaussian variances σ_c^2 and σ_u^2 are set as model inputs to determine the 2D surface slope distribution instead of wind speed and direction. The slope variance for a 1D surface slope probability distribution is then automatically given as $\sigma^2 = \sigma_u^2 + \sigma_c^2$. The advantage of this approach is that the slope variances do not depend on parameterizations in terms of wind speed, and that it gives more freedom to reproduce the measured 2D glint pattern by varying σ_c and σ_u.

Besides the assumption of Gaussian surfaces, the surface multiple reflectance and polarization also influence glint reflectance [34]. For simplicity, they are ignored in this paper because multiple reflectance only becomes important for very low solar elevations, while polarization effects are relatively unimportant at 1035 nm due to a weak molecular (and aerosol) scattering.

3. REFLECTANCE MEASUREMENT AND RETRIEVAL

A. NASA CAR Measurement

The measurements used in this paper were obtained under clear sky conditions from the NASA CAR deployed aboard the

University of Washington Convair 580 (CV-580) research aircraft [35]. The CAR is an airborne multiwavelength scanning radiometer that measures scattered light in 14 spectral bands between 0.34 and 2.30 μm. To measure BRDFs, the airplane flew in a circle about 3 km in diameter, taking roughly 2–3 min to complete an orbit about 200 m above the surface. A servo control system is installed to allow the instrument to point at any angle from zenith to nadir, and to compensate for variations in airplane roll angle down to a fraction of a degree. Multiple circular orbits were acquired over a selected surface so that average BRDFs would be smooth. Radiometric calibration was performed at Goddard Space Flight Center prior to and just after the field experiment and a linear change between them is assumed. The calibration ratio postflight/preflight averaged is about 0.98. For more details about the BRDF measurements, see [35] and the NASA official link (http://car.gsfc.nasa.gov/).

CAR measurements provide accurate BRDFs for all geometry angles including zenith viewing angles from the nadir ($\theta = 0°$) to the horizon direction ($\theta = 90°$) over all relative azimuth angles (0 – 360°). The resolution for both polar and azimuth angles is 1°. The BRDF measurements are also accompanied by concurrent measurements of atmospheric aerosol optical thickness above the airplane and wind speeds from the NOAA Marine Environmental Buoy Database.

B. Retrieval Method

To find the best match between model-simulated and CAR-measured reflectances, we use a Gauss–Newton/Levenberg–Marquardt algorithm, which is a nonlinear regression method to minimize the cost function, or the residual defined as a sum of model and measurement differences. Here the model inputs, stored in the vector **x**, include the following four retrieval parameters: two Gaussian variances σ_c^2 and σ_u^2, the wind direction, and the optical thickness τ_{mix} of the layer with a mixed population of aerosols and molecules. The RT model is used as the forward model **F(x)** and reflectance measurements are stored in the vector **y**. We then invert the forward model to retrieve the model inputs **x**. The geometry angles are read from the measurement data. The kth iteration of **x** is

$$\mathbf{x}_{k+1} = \mathbf{x}_k + [\mathbf{J}_k^T\mathbf{J}_k + \gamma_k I]\mathbf{J}_k^T(\mathbf{F}(\mathbf{x}_k) - \mathbf{y}_k), \qquad (13)$$

where the vector **J** contains the Jacobians of the forward model, I is identity matrix, and γ_k ($0 \leq \gamma_k \leq \infty$) is the Levenberg parameter, which is chosen at each iterative step to minimize the residual. If $\gamma_k = 0$ we have a classic Gauss–Newton method, while if γ_k is large we have a steepest descent method.

4. RESULTS AND DISCUSSION

A. Simulation Results of Reflectance

Figure 1 shows a comparison of model-simulated and measured reflectance at 1036 nm on four different days covering conditions of different water surface roughness. Despite measurement oscillations, Fig. 1 shows that model-simulated results in general agree very well with the measurements, reproducing the main characteristics of the glint patterns under all four wind conditions. Both the shapes of the simulated glint ellipses and their tilts are generally well matched with the measurements.
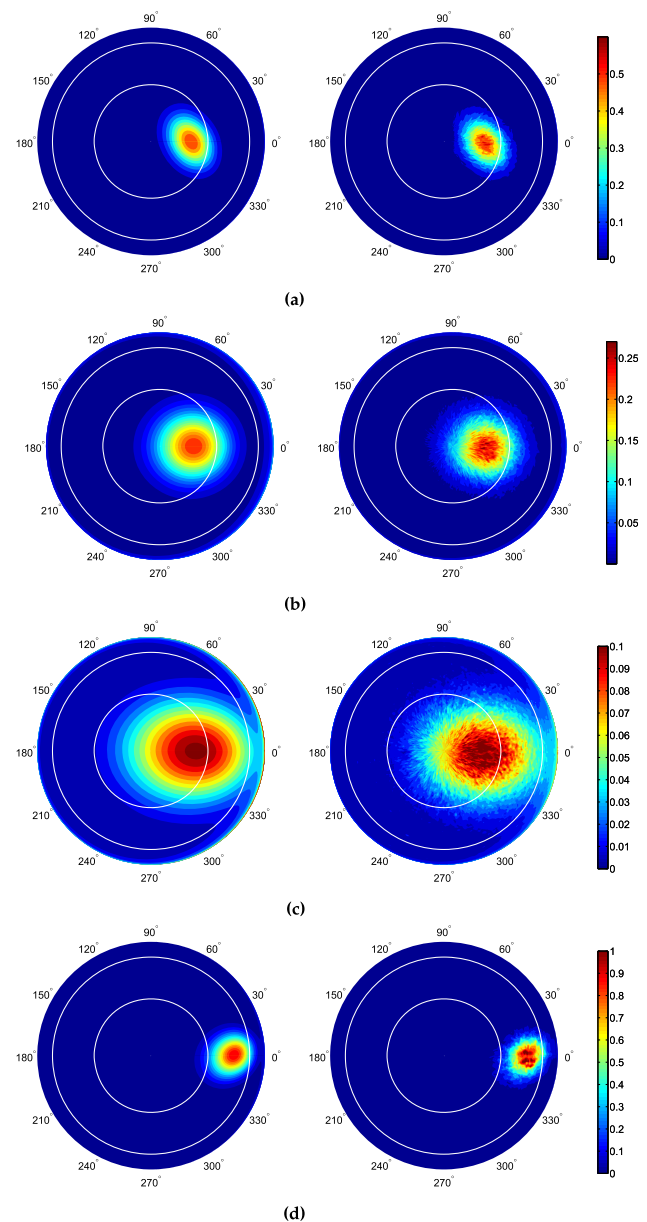

Fig. 1. Comparison between model-simulated (left) and measured reflectances (right) for different days in 2001. The inner white circles are for view zenith angles 30° and 60°. (a) 10 July, (b) 17 July, (c) 26 July, and (d) 02 August.

Figure 2 shows the same data as in Fig. 1 but for the principal plane, the perpendicular plane, and planes at ±45° axis. It is clear from Fig. 2 that the magnitude of the highest reflectance peak in the principal plane is well simulated. This agreement proves that our RT model can simulate the real ocean glint reflectance successfully.

In Fig. 2 disagreements begin to appear in the planes perpendicular and at 45° axis. The reason is partly that the reflectance in such directions may already be outside of the glint patterns, with its magnitude much smaller compared with the glint peak (e.g., "02 August"). Another possible reason for the disagreement is the unavoidable measurement errors, since each measurement is based on the assumption of unchanged water

surface conditions during the ~20 min measurement process, and the variation in observation conditions including the solar zenith angle, view zenith angle, airplane altitude and tilt angles,
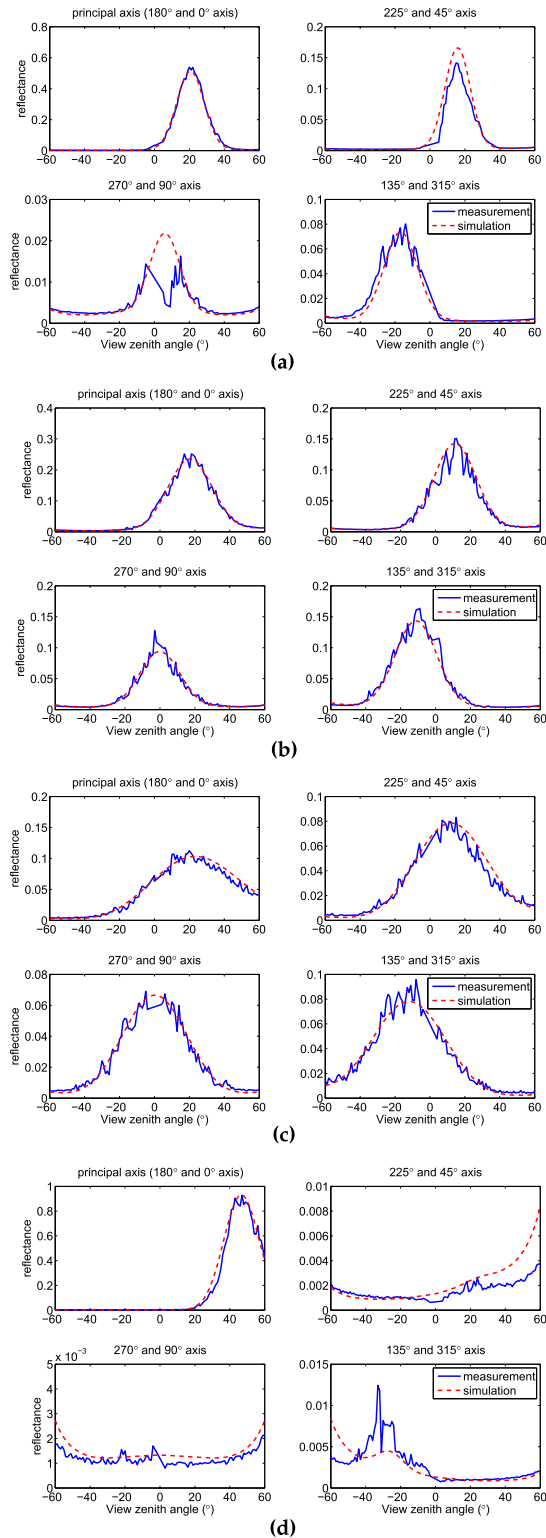

Fig. 2. Comparison between model-simulated and measured reflectances for different geometries. The measurements are in solid blue and the simulations in dashed red lines. (a) 10 July, (b) 17 July, (c) 26 July, and (d) 02 August.
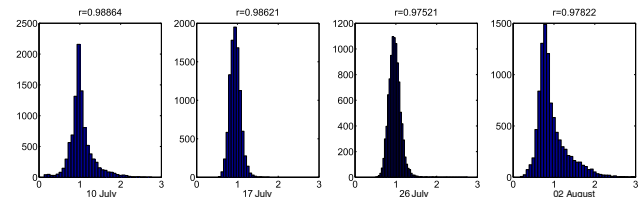

Fig. 3. Correlations and histograms of the ratio between measured and simulated reflectances.

and the influence of the airplane shadow, which is likely to be the reason for the discrepancy between theory and measurements around the nadir direction in the cross-principal plane [35].

Figure 3 shows histograms of the ratio of measured and simulated reflectances. These histogram results show the percentage differences between the measured and modeled reflectances, which also reveal general agreement. Most results are located around a ratio value of "1." However, a small part of the results are located far away from this value and again that is found from the nonglint reflectance, whose values themselves are so tiny that measurement errors are magnified.

B. Gaussian Slope Variances and the Surface Wind Speed/Direction

In Fig. 1, the shape of the elliptical glint pattern is determined by crosswind and upwind slopes (σ_c^2 and σ_u^2), while the wind direction is determined from the tilt angle. Such a tilted ellipse indicates that use of the 2D asymmetric Gaussian BRDF is necessary, and that a 1D Gaussian is insufficient to fit the angular distribution of the reflectance measurements because it averages those slopes ($\sigma^2 = \sigma_c^2 + \sigma_u^2$) to give only a circular glint pattern. Figure 4 shows a comparison of 1D and 2D results for the case "10 July." We can see that model simulations based on a 1D Gaussian BRDF are unable to match the measured tilted elliptical glint pattern and thus make them unsuitable for use in the data analysis.

As described in Section 2, we assume Gaussian distributions of the BRDF in the RT model rather than applying a "glint model." The water surface slopes σ_c^2 and σ_u^2 are then obtained through the nonlinear regression method discussed in Section 3. Nevertheless, a glint model can be used to estimate the wind speed once we know the surface slopes. Here the 1D or 2D Cox–Munk model (without the Gram–Charlier expansion) is applied because it is still one of the most reliable glint models available [9]. By inverting the following linear relations between wind speed and surface slope variances
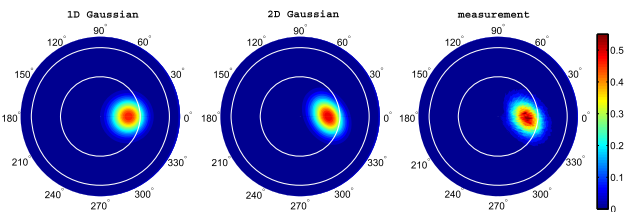

Fig. 4. Comparison between model-simulated reflectances assuming a 1D Gaussian BRDF (left), a 2D Gaussian BRDF (middle), and measurements (right) obtained on 10 July.

$$\sigma_c^2 = 0.003 + 0.00192 \, W \pm 0.002, \tag{14}$$

$$\sigma_u^2 = 0.000 + 0.00316 \, W \pm 0.004, \tag{15}$$

$$\sigma_c^2 + \sigma_u^2 = 0.003 + 0.00512 \, W \pm 0.004, \tag{16}$$

the wind speed W at 10 m above the ocean surface is obtained. Table 1 shows the retrieved slopes, wind direction, and the wind speeds inverted from the 1D/2D Cox–Munk glint model.

In Table 1 there are wind speed$_c$ and speed$_u$ for the 2D wind speed. The reason is that for a 2D glint model, the wind speed could be derived either from crosswind slope variances σ_c [Eq. (14)] or from upwind slope variances σ_u [Eq. (15)], and if the glint model is satisfied, those two values should be close to each other and constitute a possible range of the actual wind speed. This range is just what we see in Table 1, with wind speed$_c$ obtained from Eq. (14) being close to wind speed$_u$ obtained from Eq. (15). This behavior proves that the water surface slopes obtained from the model simulations are consistent with the Cox–Munk glint model.

The wind direction in Table 1 is found to be in the direction of the minor axis of the elliptical glint pattern for low wind speeds and in the direction of the major axis for high wind speeds. The high/low wind speed boundary value is around W = 2.6 m/s according to the Cox–Munk model, for which the elliptical pattern becomes circular with crosswind and up-wind slopes [Eqs. (14) and (15)] being equal. This circular glint pattern is evident in Fig. 1(b) "17 July" when the wind speed was about 3.7 m/s, which is close to the boundary value.

Associated with the BRDF observations, wind speed measurements are obtained from the NOAA Marine Environmental Buoy database [35]. Assuming a classical log wind vertical profile [36], we may use an altitude scaling algorithm to scale the wind speed measured at the aircraft altitude to the corresponding wind speed at 10 m above the ocean surface. In Fig. 5 we show the retrieved slope variances versus the

measured wind speeds and their values obtained from the Cox–Munk glint model. The retrieved variances are found to deviate from the mean value obtained from the Cox–Munk glint model, and this deviation is essential in order to match the glint patterns in Figs. 1(a)–1(d). The existence of deviations also explains the advantage of setting slope variances as RT model inputs instead of wind speed provided by the Cox–Munk glint model.

C. Aerosol Optical Thickness

The CAR data include measurements of aerosol optical thickness (AOT) above the airplane obtained by the Ames Airborne Tracking Sunphotometer (AATS) instrument deployed on the aircraft [35,37]. In the model simulations we assumed a 2 km mixed layer (molecules and aerosols). We also assumed that the airplane is inside the mixed layer and at a height such that 90% of the aerosols are above it because the airplane altitude was about 200 m during the BRDF measurements presented by Gatebe *et al.* [35].

Figure 6 shows a comparison between retrieved and AATS-measured AOT at 1036 nm. The retrieved AOT is larger, but both follow the same trend. This discrepancy may be due to our assumption of a homogenous mixing of the "aerosol-molecule" layer with a fixed 90/10% aerosol ratio. Nevertheless, this result indicates that our retrieval reflects the correct direction of aerosol variation in the atmosphere under different ocean surface roughness conditions.

D. Reproducing the Reflectance in 472, 672, and 870 nm

The sea surface roughness information retrieved from the infrared channel at 1036 nm can be directly applied to the visible and NIR wavelengths (472, 672, and 870 nm) to improve the ocean color retrieval in the sun glint area, since the surface information (σ_c^2, σ_u^2, σ^2, and wind direction) is independent of the wavelength. In Fig. 7 we show a comparison between model-simulated and CAR-measured reflectances in the visible

Table 1. Retrieved Water Surface Slopes, Wind Direction (°), and Wind Speed (m/s)

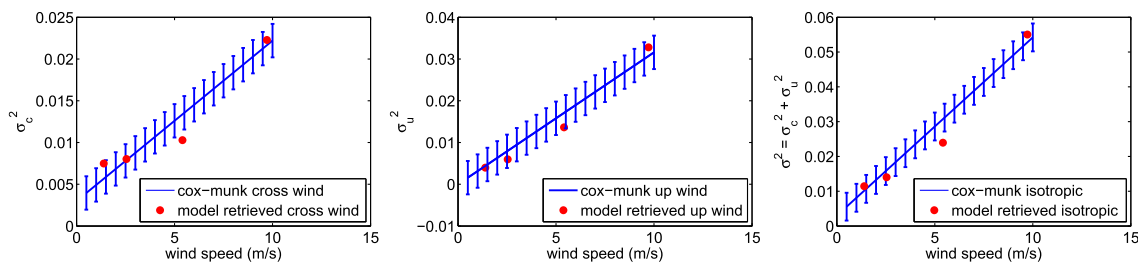| Date	σ_c^2	σ_u^2	Wind Speed$_c$ | Wind Speed$_u$	1D Wind Speed	Wind Direction
10 July	0.00747	0.00399	2.29 | 1.23	1.61	31.09
17 July	0.01028	0.01162	3.79 | 3.68	3.70	1.92
26 July	0.02228	0.03278	10.04 | 10.37	10.17	357.25
02 August	0.00802	0.00602	2.61 | 1.90	2.16	313.48

Fig. 5. Comparison between model-simulated slope variances and the Cox–Munk glint model. The wind speeds are obtained from the measurements after height scaling. The error bar from the Cox–Munk glint model is the standard deviation of surface slopes variances [0.002 from Eq. (14) and 0.004 from Eqs. (15) and (16)].
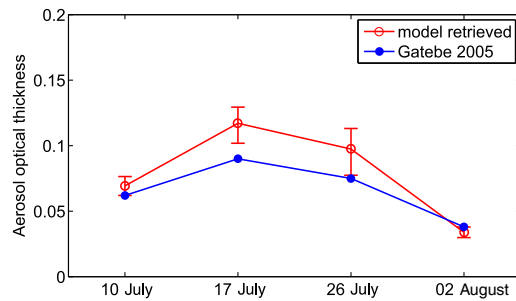
Fig. 6. Aerosol optical thickness. Retrieved results compared with AATS measurements at 1036 nm (Gatebe *et al.* 2005 [35]). The range of the error bar is computed from assuming ±10% of the measurement errors.

channels for measurements obtained on 10 July, 2001. In this simulation, we used the sea surface roughness information obtained from the CAR 1036 nm channel as described above and apply DISORT3 to compute the glint contribution in the visible channels. The aerosol and ocean parameters were retrieved from the nonglint area (viewing angles 20–60 deg and relative azimuth angles 120–240 deg) with the multiangle reflectances in three CAR channels at 472, 682, and 870 nm. AccuRT, a radiative transfer model for the coupled atmosphere–ocean system, based on the discrete-ordinate method [38–42] was used with an optimization technique to retrieve the aerosol and water constituent parameters simultaneously [43–45]). The aerosol model of Ahmad *et al.* [31] and the CCRR (CoastColour Round Robin) bio-optical model [46] were used in AccuRT for this retrieval. In this case, the retrieved aerosol optical depth at 870 nm was 0.086 and the Ångstrøm coefficient (472–870 nm) was 1.463. In the ocean the retrieved chlorophyll concentration was $0.67 \text{ mg} \cdot \text{m}^{-3}$, the colored dissolved organic matter absorption coefficient at 443 nm was 0.07 m^{-1}, and the mineral particle concentration was $0.009 \text{ g} \cdot \text{m}^{-3}$. When we applied these retrieved results to the BRDF simulation, we got a very good match to the CAR measurements, especially in the glint area, except for the discrepancy around the nadir direction in the cross-principal plane, which is likely due to the airplane shadow in the observations [35]. This good match implies that the glint information retrieved in the infrared at 1.036 nm from DISORT3 can be used in ocean color remote sensing to estimate the glint contribution in the visible and NIR ocean channels.

E. Discussion on the Diffuse Light Reflectance

Besides the direct solar beam reflectance (sun glint), diffuse or multiply scattered solar light generated by scattering from atmospheric molecules and particles can also be reflected by the rough ocean surface and produces a glint signal, which is normally called "sky glint" [1]. The "sky glint" contribution has been considered in some atmospheric correction algorithms, e.g., by Gao *et al.* [20], but in the SeaDAS algorithm the effect of ocean surface roughness has been included only the Rayleigh lookup tables. Below we will apply DISORT3 to quantify the contribution due to "sky glint" at various wavelengths. Since multiple light scattering is automatically
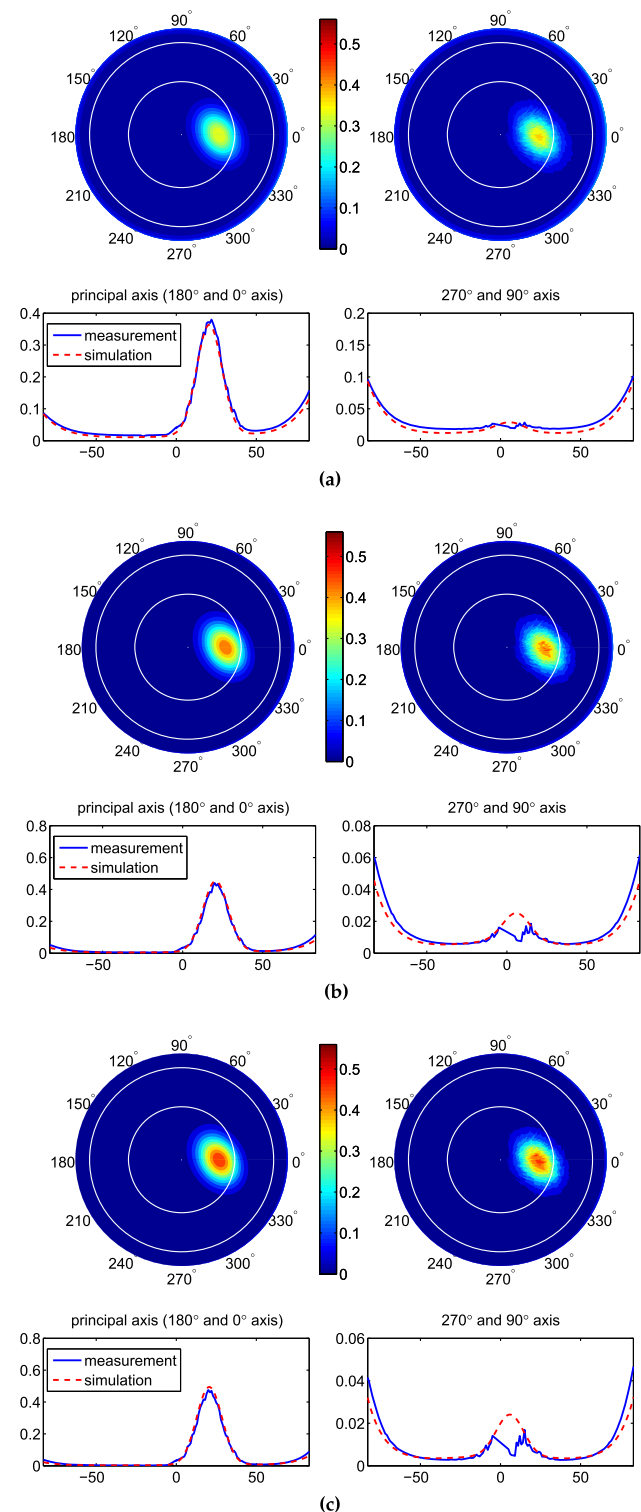

Fig. 7. Comparison between model-simulated and measured reflectances for case 10 July at wavelengths 472, 682, and 870 nm. The left contour plots are from the simulations and the right contour plots are from the measurements.

included in DISORT3, the contribution of diffuse light reflectance can easily be computed by removing the singly scattered reflectance from the total reflectance.
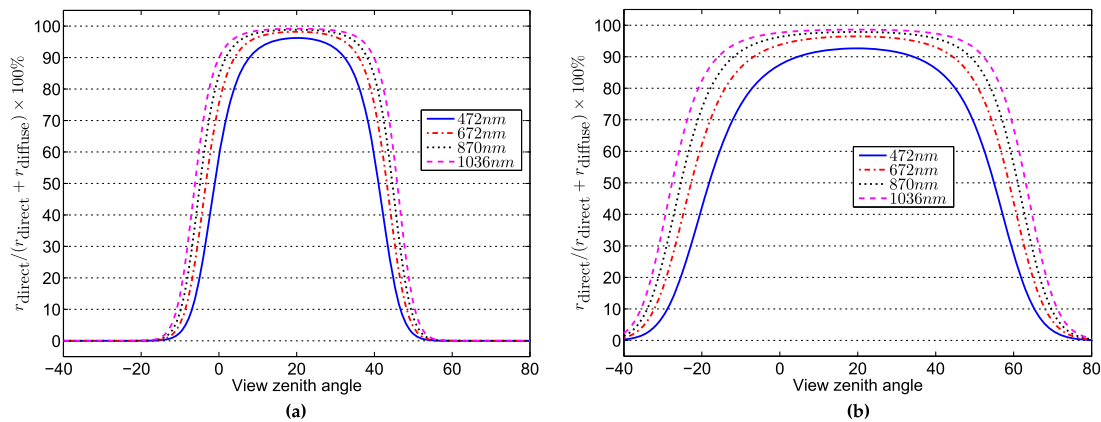
Fig. 8. Percentage contribution of solar beam reflectance just above sea surface for case 10 July at wavelengths 472, 682, 870, and 1036 nm. (a) Contribution of the direct beam reflectance (%) for a wind speed of 2 m/s. (b) Contribution of the direct beam reflectance (%) for a wind speed of 8 m/s; otherwise the setup is the same as in (a).

To distinguish the glint contribution due to direct beam and diffuse skylight, we define r_{direct} as the direct solar beam reflectance just above sea surface, and r_{diffuse} as the diffuse light reflectance. Then $r_{\text{direct}}/(r_{\text{direct}} + r_{\text{diffuse}}) \times 100\%$ gives the percentage contribution from direct beam reflectance just above the sea surface that is commonly used in current algorithms. Figure 8(a) shows results for the 10 July case in the principal plane where the glint is centered at 20° and the retrieved wind speed is about 2 m/s. The results indicate a loss of more than about 4% intensity around the glint center in 472 nm when the multiple scattering is strong and a gradual decrease as the wavelength increases. The diffuse beam reflectance could almost be ignored in the 1036 nm IR channel. Assuming the same situation but applying a more general surface roughness that is equivalent to a wind speed of 8 m/s, Fig. 8(b) shows the diffuse beam reflectance is doubled and contributed more about 8% for 472 nm and 4% for 672 nm around the glint center, because the wind-roughened sea surface spread the direct beam reflectance. Also note that the glint loss becomes even much larger at the flanks of the glint profile. For example, 50% glint loss could be found at the −20° viewing angle seen in Fig. 8(b).

These results indicate that diffuse light ("sky glint") reflectance is important and should be considered in the visible bands where molecular and particle scattering produce stronger diffuse light than at longer wavelengths. Sky glint should also be considered for high wind speeds when the sea surface becomes rougher.

5. SUMMARY AND CONCLUSION

The latest version of the DISORT code (DISORT3 [23]) was modified to simulate ocean glint reflectance and retrieve surface roughness such that for the first time simulations did successfully match airplane BRDF measurements from NASA's CAR at the 1036 nm wavelength. The modification brings in a pseudo-two-dimensional Gaussian BRDF approximation that uses (1) a 2D Gaussian surface slope distribution for singly scattered light, and keeps (2) a 1D Gaussian surface slope distribution for multiply scattered light. This approximation is implemented through a postprocessing correction that can generally be applied to any other asymmetric type of BRDF.

Model inputs consisting of upwind and crosswind slope variances, wind direction, and AOT, are retrieved through forward-inverse modeling and the retrieval results look very reasonable. The retrieved slope variances agree well with the slope variances derived from the Cox–Munk glint model using measured wind speeds. Consistent trends of variation are found for the retrieved AOT. We then show that the glint parameters (slope variances and wind direction) can be applied to estimate the glint contribution at visible and NIR wavelengths, and that a very good match can be obtained between model-simulated and measured reflectances.

An advantage of RT simulations of glint reflectance is its inclusion of the surface reflectance from the diffuse or multiply scattered light that is due to scattering by atmospheric molecules and aerosols. The diffuse light reflectance ("sky glint") gives an additional glint signal besides "sun glint" resulting from the direct beam reflectance. Simulations of the 10 July case show that the diffuse glint contributes more than 4% at 472 nm and more than 8% for the same case as the wind speed increased from 2 m/s to 8 m/s. This finding indicates that the diffuse light reflectance should be considered in the visible bands, especially for large wind speeds when the sea surface is roughened.

The validated RT model provides a valuable approach to study the glint problem besides the many current correction methods which have attempted to remove the sun glint contribution using a crude glint model that ignores multiple scattering. The modified DISORT3 could be used to determine a more accurate glint contribution that includes a 2D surface BRDF and the contribution from diffuse light reflectance. The RT model can also be used to conduct sensitivity studies aimed at improving our understanding of glint reflectance, and to produce synthetic data that could be used to test and improve glint correction algorithms for application to current and future ocean color remote sensing data. Finally, the pseudo-2D BRDF and glint reflectance method developed in this paper can be implemented in RT models for the coupled

atmosphere–ocean system to give a more complete and accurate simulation of the remote sensing reflectance.

REFERENCES

1. S. Kay, J. D. Hedley, and S. Lavender, "Sun glint correction of high and low spatial resolution images of aquatic scenes: a review of methods for visible and near-infrared wavelengths," Remote Sens. **1**, 697–730 (2009).
2. M. Wang and S. W. Bailey, "Correction of sun glint contamination on the SeaWiFS ocean and atmosphere products," Appl. Opt. **40**, 4792–4798 (2001).
3. F. Steinmetz, P.-Y. Deschamps, and D. Ramon, "Atmospheric correction in presence of sun glint: application to MERIS," Opt. Express **19**, 9783–9800 (2011).
4. H. Fukushima, K. Suzuki, L. Li, N. Suzuki, and H. Murakami, "Improvement of the adeos-ii/gli sun-glint algorithm using concomitant microwave scatterometer-derived wind data," Adv. Space Res. **43**, 941–947 (2009).
5. J. Hedley, A. Harborne, and P. Mumby, "Technical note: simple and robust removal of sun glint for mapping shallow-water benthos," Int. J. Remote Sens. **26**, 2107–2112 (2005).
6. C. Hu, "An empirical approach to derive MODIS ocean color patterns under severe sun glint," Geophys. Res. Lett. **38**, 1–5 (2011).
7. C. Cox and W. Munk, "Measurement of the roughness of the sea surface from photographs of the sun's glitter," J. Opt. Soc. Am. **44**, 838–850 (1954).
8. Y. Hu, K. Stamnes, M. Vaughan, J. Pelon, C. Weimer, D. Wu, M. Cisewski, W. Sun, P. Yang, B. Lin, A. Omar, D. Flittner, C. Trepte, D. Winker, G. Gibson, and M. Santa-Maria, "Sea surface wind speed estimation from space-based lidar measurements," Atmos. Chem. Phys. **8**, 3593–3601 (2008).
9. H. Zhang and M. Wang, "Evaluation of sun glint models using MODIS measurements," J. Quant. Spectrosc. Radiat. Transfer **111**, 492–506 (2010).
10. J. Wu, "Mean square slopes of the wind-disturbed water surface, their magnitude, directionality, and composition," Radio Sci. **25**, 37–48 (1990).
11. E. J. Walsh, D. C. Vandemark, C. A. Friehe, S. P. Burns, D. Khelif, R. N. Swift, and J. F. Scott, "Measuring sea surface mean square slope with a 36-ghz scanning radar altimeter," J. Geophys. Res. **103**, 12587–12601 (1998).
12. J. A. Shaw and J. H. Churnside, "Scanning-laser glint measurements of sea-surface slope statistics," Appl. Opt. **36**, 4202–4213 (1997).
13. J. Wu, "Effects of atmospheric stability on ocean ripples: a comparison between optical and microwave measurements," J. Geophys. Res. **96**, 7265–7269 (1991).
14. H. R. Gordon, "Atmospheric correction of ocean color imagery in the earth observation system era," J. Geophys. Res. **102**, 17081–17106 (1997).
15. M. Wang, "The Rayleigh lookup tables for the SeaWiFS data processing: accounting for the effects of ocean surface roughness," Int. J. Remote Sens. **23**, 2693–2702 (2002).
16. J. Chowdhary, B. Cairns, M. I. Mishchenko, P. V. Hobbs, G. F. Cota, J. Redemann, K. Rutledge, B. N. Holben, and E. Russell, "Retrieval of aerosol scattering and absorption properties from photopolarimetric observations over the ocean during the clams experiment," J. Atmos. Sci. **62**, 1093–1117 (2005).
17. J. Chowdhary, B. Cairns, and L. D. Travis, "Contribution of water-leaving radiances to multiangle, multispectral polarimetric observations over the open ocean: bio-optical model results for case 1 waters," Appl. Opt. **45**, 5542–5567 (2006).
18. J. Chowdhary, B. Cairns, F. Waquet, K. Knobelspiesse, M. Ottaviani, J. Redemann, L. Travis, and M. Mishchenko, "Sensitivity of

19. multiangle, multispectral polarimetric remote sensing over open oceans to water-leaving radiance: analyses of RSP data acquired during the MILAGRO campaign," Remote Sens. Environ. **118**, 284–308 (2012).
19. M. Ottaviani, R. Spurr, K. Stamnes, W. Li, W. Su, and W. Wiscombe, "Improving the description of sunglint for accurate prediction of remotely sensed radiances," J. Quant. Spectrosc. Radiat. Transfer **109**, 2364–2375 (2008).
20. B.-C. Gao, M. J. Montes, Z. Ahmad, and C. O. Davis, "Atmospheric correction algorithm for hyperspectral remote sensing of ocean color from space," Appl. Opt. **39**, 887–896 (2000).
21. B.-C. Gao, HyspIRI Visible to Short Wavelength Infrared (VSWIR) Water Leaving Reflectance Algorithm Theoretical Basis Document (ATBD) (2010), https://hyspiri.jpl.nasa.gov/downloads/Algorithm_ Theoretical_Basis/HyspIRI_Gao_ATBD-VSWIR_Water_8_2010_ 101109.pdf.
22. Z. Ahmad and R. S. Fraser, "An iterative radiative transfer code for ocean-atmosphere systems," J. Atmos. Sci. **39**, 656–665 (1982).
23. Z. Lin, S. Stamnes, Z. Jin, I. Laszlo, S.-C. Tsay, W. Wiscombe, and K. Stamnes, "Improved discrete ordinate solutions in the presence of an anisotropically reflecting lower boundary: upgrades of the DISORT computational tool," J. Quant. Spectrosc. Radiat. Transfer **157**, 119–134 (2015).
24. Z. Jin, T. P. Charlock, K. Rutledge, K. Stamnes, and Y. Wang, "Analytical solution of radiative transfer in the coupled atmosphere-ocean system with a rough surface," Appl. Opt. **45**, 7443–7455 (2006).
25. K. Stamnes, S.-C. Tsay, W. Wiscombe, and K. Jayaweera, "Numerically stable algorithm for discrete-ordinate-method radiative transfer in multiple scattering and emitting layered media," Appl. Opt. **27**, 2502–2509 (1988).
26. V. Rozanov, A. Rozanov, A. Kokhanovsky, and J. Burrows, "Radiative transfer through terrestrial atmosphere and ocean: software package SCIATRAN," J. Quant. Spectrosc. Radiat. Transfer **133**, 13–71 (2014).
27. P.-W. Zhai, Y. Hu, J. Chowdhary, C. R. Trepte, P. L. Lucker, and D. B. Josset, "A vector radiative transfer model for coupled atmosphere and ocean systems with a rough interface," J. Quant. Spectrosc. Radiat. Transfer **111**, 1025–1040 (2010).
28. R. Spurr, "Lidort and vlidort: linearized pseudo-spherical scalar and vector discrete ordinate radiative transfer models for use in remote sensing retrieval problems," in *Light Scattering Reviews 3* (Springer, 2008), pp. 229–275.
29. Light and Life Laboratory (2015), http://lllab.phy.stevens.edu/disort.
30. NOAA, "US standard atmosphere, 1976," Tech. Rep. NOAA-S/T (1976).
31. Z. Ahmad, B. A. Franz, C. R. McClain, E. J. Kwiatkowska, J. Werdell, E. P. Shettle, and B. N. Holben, "New aerosol models for the retrieval of aerosol optical thickness and normalized water-leaving radiances from the SeaWiFS and MODIS sensors over coastal regions and open oceans," Appl. Opt. **49**, 5545–5560 (2010).
32. T. Nakajima and M. Tanaka, "Algorithms for radiative intensity calculations in moderately thick atmospheres using a truncation approximation," J. Quant. Spectrosc. Radiat. Transfer **40**, 51–69 (1988).
33. K. Masuda, "Effects of the speed and direction of surface winds on the radiation in the atmosphere-ocean system," Remote Sens. Environ. **64**, 53–63 (1998).
34. C. D. Mobley, "Polarized reflectance and transmittance properties of windblown sea surfaces," Appl. Opt. **54**, 4828–4849 (2015).
35. C. K. Gatebe, M. D. King, A. I. Lyapustin, G. T. Arnold, and J. Redemann, "Airborne spectral measurements of ocean directional reflectance," J. Atmos. Sci. **62**, 1072–1092 (2005).
36. H. Charnock, "Wind stress on a water surface," Q. J. R. Meteorolog. Soc. **81**, 639–640 (1955).
37. J. Redemann, B. Schmid, J. Eilers, R. Kahn, R. Levy, P. Russell, J. Livingston, P. Hobbs, W. Smith, Jr., and B. Holben, "Suborbital measurements of spectral aerosol optical depth and its variability at subsatellite grid scales in support of clams 2001," J. Atmos. Sci. **62**, 993–1007 (2005).
38. Z. Jin and K. Stamnes, "Radiative transfer in nonuniformly refracting media such as the atmosphere/ocean system," Appl. Opt. **33**, 431–442 (1994).
39. G. E. Thomas and K. Stamnes, *Radiative Transfer in the Atmosphere and Ocean*, 2nd ed. (Cambridge University, 2002).

40. B. Hamre, S. Stamnes, K. Stamnes, and J. J. Stamnes, "C-DISORT: a versatile tool for radiative transfer in coupled media like the atmosphere-ocean system," AIP Conf. Proc. **1531**, 923–926 (2013).

41. B. Hamre, S. Stamnes, J. J. Stamnes, and K. Stamnes, "A versatile tool for radiative transfer simulations in the coupled atmosphere-ocean system: introducing accurt," in *Ocean Optics XXII* (2014), pp. 26–31.

42. K. Stamnes and J. J. Stamnes, *Radiative Transfer in Coupled Environmental Systems: An Introduction to Forward and Inverse Modeling* (Wiley-VCH, 2015).

43. W. Li, K. Stamnes, R. Spurr, and J. Stamnes, "Simultaneous retrieval of aerosol and ocean properties by optimal estimation: SeaWiFS case studies for the Santa Barbara channel," Int. J. Remote Sens. **29**, 5689–5698 (2008).

44. Y. Fan, W. Li, K. J. Voss, C. K. Gatebe, and K. Stamnes, "A neural network method to correct bidirectional effects in water-leaving radiance," Appl. Opt. **55**, 10–21 (2015).

45. Y. Fan, W. Li, K. Stamnes, J. J. Stamnes, and K. Sørensen, "Simultaneous retrieval of aerosol and marine parameters in coastal areas using a coupled atmosphere-ocean radiative transfer model," in *Proceedings of the Sentinel-3 for Science Workshop* (ESA, 2015).

46. K. Ruddick, DUE CoastColour Round Robin Protocol, Version 1.2 (2010). http://coastcolour.org/documents/Coastcolour-RRP-v1.2.pdf.